Fabrication of phosphate hybrid materials with remarkably catalytic hydrogen generation by Dr Xiulin Yang from Clean Energy Lab at Guangxi Normal University.

Hierarchically structured rugae-like RuP_3–CoP arrays as robust catalysts synergistically promoting hydrogen generation

A novel rugae-like RuP_3-CoP nanostructure decorated Ni foam demonstrated an outstanding catalytic performance with a high turnover frequency and long term stability towards hydrolytic hydrogen generation. The outstanding catalytic performance could be due to the unique morphology and excellent charge transfer property along with the synergy between RuP_3 and CoP.

As featured in:

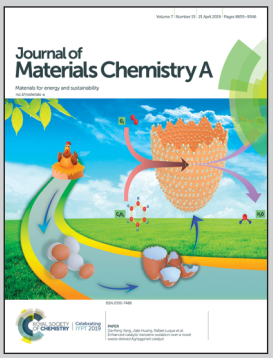

See Tayirjan Taylor Isimjan, Xiulin Yang *et al.*, *J. Mater. Chem. A*, 2019, **7**, 8865.

ROYAL SOCIETY OF CHEMISTRY | Celebrating IYPT 2019

rsc.li/materials-a

Registered charity number: 207890

Journal of Materials Chemistry A

PAPER

View Article Online
View Journal | View Issue

Cite this: J. Mater. Chem. A, 2019, 7, 8865

Hierarchically structured rugae-like RuP_3–CoP arrays as robust catalysts synergistically promoting hydrogen generation†

Jingya Guo,[a] Chongbei Wu,[a] Jifang Zhang,[a] Puxuan Yan,[a] Jianniao Tian,[a] Xingcan Shen,[a] Tayirjan Taylor Isimjan *[b] and Xiulin Yang *[a]

Received 6th November 2018
Accepted 14th January 2019

DOI: 10.1039/c8ta10695a

rsc.li/materials-a

Designing a highly active and stable catalyst for $NaBH_4$ hydrolysis is a key step towards overcoming the challenges of hydrogen storage. Herein, we have developed a controllable strategy to fabricate a series of hierarchically structured cobalt-ruthenium-phosphide arrays on nickel foam (Co–Ru–P@NF) as a highly efficient and stable catalyst for hydrogen generation from $NaBH_4$ hydrolysis in alkaline media. SEM and TEM analyses show that the interconnected rugae-like Co–Ru–P arrays are vertically grown on the surface of Ni foam, together with uniformly distributed RuP_3 nanoclusters on the surface of CoP nanosheets. More importantly, the optimized Co–Ru–P@NF catalyst exhibits an outstanding catalytic performance on $NaBH_4$ hydrolysis in alkaline media with a high turnover frequency (TOF) of 2123.6 mol_{H_2} min^{-1} $mol_{Ru}{}^{-1}$ at 25 °C, which is one of the highest known so far. Furthermore, the exceptional catalytic performance is in line with the outcome of low activation energy (40.3 kJ mol^{-1}). Additionally, the catalyst also shows a high stability with less than 8.0% lost after 5 consecutive cycles. The superior catalytic performance is ascribed to the synergetic effect between RuP_3 and CoP species resulting in a significant electron transfer effect, together with the unique morphologies associated with a large specific surface area and open-channels for effective solute transport/adsorption and H_2 gas emissions.

1. Introduction

Dealing with the continuously growing energy demand resulting from fossil fuel depletion and a related environmental crisis is prompting vigorous research in the field of clean and sustainable alternative energy sources.[1–3] Molecular hydrogen with the highest gravimetric energy density (120 MJ kg^{-1}) is regarded as a promising candidate.[4–6] However, H_2 storage and transportation are two main hindrances to realize a H_2 economy.[7–9] H_2 can be stored using both physical and chemical methods where the H_2 either is adsorbed on highly porous materials such as MOFs and porous carbon, which requires extremely low temperature, or stored as metal-hydride complexes including boron hydrides ($NaBH_4$, NH_3BH_3 and $LiBH_4$) which has the advantages of high H_2 content (10–20%), high water solubility and stability at room temperature as well as non-toxicity.[10–12] Nevertheless, boron hydride hydrolysis generally suffers from sluggish kinetics.[13] Therefore, developing a low cost and high-performance catalyst becomes an essential step to promote H_2 storage through boron hydrides. Although noble metal catalysts such as Pt/CeO_2–$Co_7Ni_2O_x$,[14] Pd/PD-ZIF-67,[15] Pt/3D SiC,[16] $Pt_{58}Ni_{33}Au_9$,[17] Pt/mesoporous silica,[18] Ru@SiO_2,[19] Ni–Ru,[20] Rh/Ni BNPs,[21] $Co_{0.8}$–$Ag_{0.2}$–B,[22] *etc.* exhibit high catalytic performances, they are also limited by their cost. As a result, developing transition metal (Co, Fe, and Ni) based catalysts has become the main focus for boron hydride hydrolysis. Recent studies have revealed a significant enhancement in the catalytic performance of transition metal catalysts by incorporating foreign elements including B and P.[23–26] The improvement of the catalytic performance could be due to electron transfer from B or P to the vacant d-orbital of the metal and the electron enriched metal sites further donate electrons to the surface attached hydrogen atoms thereby accelerating detachment of the surface adsorbed hydrogen atoms.[27] Furthermore, for metal phosphates, in particular, introducing additional foreign metals can further increase the catalytic performance.[28,29] However, the actual catalytic performance is largely altered by the catalyst preparation, microstructure engineering, surface area, and catalyst support. In general, porous supports such as nickel foam (NF), copper foam, titanium sheets, porous carbon, Al_2O_3, SiO_2, and TiO_2 not only provide a high surface area but also inhibit catalyst aggregation

[a]Key Laboratory for the Chemistry and Molecular Engineering of Medicinal Resources, Ministry of Education of China, College of Chemistry and Pharmacy, Guangxi Normal University, Guilin 541004, People's Republic of China. E-mail: xiulin.yang@kaust.edu.sa

[b]Saudi Arabia Basic Industries on (SABIC) at King Abdullah University of Science and Technology (KAUST), Saudi Arabia. E-mail: isimjant@sabic.com

† Electronic supplementary information (ESI) available: Fig. S1–S13 and Tables S1–S3 give more details on the characterization of our synthesized materials and their catalytic performance data; additional photographs, XRD, SEM, XPS and catalytic performance data (PDF). See DOI: 10.1039/c8ta10695a

thereby improving both activity and stability.[30–33] Compared to powder catalysts, the metal sheet supported catalysts can be easily separated from the solution and used as an on/off switch for on-demand hydrogen production.[34] Liu and co-workers found that CoP nanowire arrays integrated on a Ti mesh showed a high hydrogen generation rate for hydrolytic dehydrogenation of $NaBH_4$ in alkaline solutions.[34] Moreover, Sun and co-workers also reported that Fe-doped CoP nanoarrays on Ti foil exhibited a high hydrogen generation rate and low activation energy for hydrolytic dehydrogenation of $NaBH_4$ in basic media.[29] Recently, NF supports attracted a lot of attention due to their distinguished features such as a three-dimensional reticular configuration, high surface areas, high flexibility and low cost.[8,35]

Herein, we have developed a facile and controllable strategy to synthesize a novel RuP_3 coated CoP on NF hybrid catalyst where the cheapest noble metal Ru[36] was used in a small quantity in order to minimize the cost. X-ray diffraction patterns indicate that RuP_3 and CoP species are formed, and the contents of Ru and Co in the optimized catalyst are indicated to be $Co_{0.991}Ru_{0.09}P$ by ICP-AES. SEM and TEM demonstrate that rugae-like CoP arrays are grown on the skeleton of NF, and RuP_3 nanoclusters are uniformly dispersed on the CoP nanosheet surface. The optimized Co–Ru–P@NF catalyst exhibits an outstanding catalytic performance and high stability for $NaBH_4$ hydrolysis. This exceptional performance can be ascribed to the synergetic effect of RuP_3 and CoP species, along with the unique morphologies and high surface area offered by NF. Furthermore, a catalytic mechanism of $NaBH_4$ hydrolysis on the Co–Ru–P@NF hybrid catalyst was proposed.

2. Experimental section

2.1. Synthesis of Co-species@NF

Co-species nanosheet arrays on NF (Ni foam) were prepared as follows, where a piece of NF (1 cm × 1 cm × 1.6 mm) was carefully pretreated in 1.0 M HCl, deionized water and ethanol for 5 min, respectively. This was then repeated three times to confirm that the surface of NF was well cleaned.

To prepare the Co-species@NF, 1.0 mmol of $Co(NO_3)_2 \cdot 6H_2O$ was ultrasonically dissolved in 40 mL deionized water to form a uniform solution. The electrodeposition experiments were carried out at room temperature in a standard three-electrode system with NF as the working electrode, a Pt sheet as the counter electrode, and a standard SCE as the reference electrode. The applied current density was set as -10 mA cm^{-2}, and different electrodeposition times were used to control the amount of Co-species (20, 30, 40, 50 and 60 min). The resultant samples were washed with abundant deionized water and dried in air at room temperature. The loadings of Co-species on the NF surface are calculated for 3.67, 5.5, 7.34, 9.17 and 11.01 mg cm^{-2}, respectively.

2.2. Synthesis of CoRu-species@NF

50 mg of ruthenium(III) 2,4-pentanedionate was ultrasonically dispersed into 10 mL ethanol to form a homogeneous solution. Then, the solution mixture was pipetted onto the surface of Co-species@NF-60 and dried in air at room temperature. For a better comparison, different volumes of the precursors on the NF-60 surface are investigated. Moreover, precursor covered fresh NF is also studied.

2.3. Synthesis of Co–Ru–P@NF by vapor phase phosphidation

The phosphidation process was performed in a tube furnace, where NaH_2PO_2 in a porcelain boat was put in the upstream side and a series of CoRu-species/NF samples were placed next to the NaH_2PO_2 at the downstream side. The furnace was heated to 350 °C with 2 °C min^{-1} in an Ar atmosphere (20 sccm), and kept at 350 °C for 2 h. After the phosphidation, the samples were cooled down to ambient temperature in flowing Ar gas. As a comparison, the CoP@NF, RuP_3@NF and Ni_2P@NF were also prepared by a similar phosphidation process.

2.4. Catalyst characterization

The crystal structures of catalysts were analyzed by X-ray powder diffraction (XRD, Rigaku D/Max 2500 V/PC) with a sweep speed of 2.0° min^{-1}. The morphologies and microstructures of the catalysts were characterized using a scanning electron microscope (SEM, FEI Quanta 200 FEG) and transmission electron microscope (TEM, JEM-2100F). An X-ray photoelectron spectrometer (XPS, JPS-9010 Mg Kα) was used to analyze the chemical states of different elements. The specific surface area of the as-prepared product was measured on a Quantachrome Autosorb AS-1 instrument. The actual loadings of different metals in the catalyst were checked by inductively coupled plasma atomic emission spectroscopy (ICP-AES, IRIS Intrepid II XSP).

2.5. Catalytic measurements

The catalytic activity, cycle stability and activation energy of the catalytic material were obtained by the following methods. Typically, 50 mL solution mixture (containing 150 mM $NaBH_4$ + 0.4 wt% NaOH) was kept in a three-necked round-bottom flask (100 mL), which was placed in a water bath at 25 °C. The volume of H_2 was monitored by a drainage which was connected to a computer to record the instantly changed qualities of water. The catalytic reaction was started when the catalyst was added into the flask under constant magnetic stirring conditions. In order to test the recyclability of the catalyst, we continued to use the fresh $NaBH_4$ solution instead of the fully decomposed $NaBH_4$ solution for five consecutive cycles at 25 °C. After each stability test, we centrifuged the catalytic material, dried it under vacuum conditions at room temperature, and weighed the catalytic material. All experiments were repeated three times to ensure reliable results. The activation energy of the designed catalyst was evaluated in the same device in the temperature range of 25 to 45 °C.

The specific H_2 generation rate (HGR) and turnover frequency (TOF) values are calculated as follows:[34,37]

$$\mathrm{HGR} = \frac{V_{H_2O}\ (\mathrm{mL})}{t\ (\mathrm{min}) \times m\ (\mathrm{g})} \quad (1)$$

$$\mathrm{TOF} = \frac{n_{H_2}\ (\mathrm{mol})}{t\ (\mathrm{min}) \times n_{Ru}\ (\mathrm{mol})} \quad (2)$$

where V_{H_2O} is the volume of drained water, m is the total mass of the catalyst, n_{H_2} is the moles of generated H_2, n_{Ru} is the moles of Ru in the catalyst, and t is the total reaction time in minutes.

3. Results and discussion

3.1. Synthetic strategy analysis

The three dimensional Co–Ru–P@NF catalysts were prepared through three steps including electrodeposition of Co species, Ru modification and high-temperature phosphorization (Fig. 1). Initially, the Co-species were loaded on the NF surface (Co@NF) by electrodeposition at a constant current density within various time lengths. Thereafter, Ru-precursors in ethanol solution were loaded dropwise onto the surface of Co@NF. Finally, the Ru loaded Co@NFs were placed in a porcelain boat next to another porcelain boat in the upside containing NaH_2PO_2 as the phosphor source. The hierarchically structured Co–Ru–P@NF materials were prepared through vapor deposition of phosphorous under constant argon flow at 350 °C for 2 h. The metal loadings were determined by ICP-AES, which were used to calculate the TOF of H_2 generation (Table S1†). Moreover, the pictures of the sample at different stages indicate the surface transformations by various chemical treatments as shown in Fig. S1† and the weight changes of the catalysts were monitored using a precision balance to calculate the following H_2 generation rates (Table S2†).

3.2. Crystal structures and microstructure analysis

The crystal structures of the as-prepared materials are initially investigated using XRD patterns. As shown in Fig. S2a,† the electrodeposited Co-species on the NF surface are consistent with the standard XRD features of $Co(OH)_2$ (JCPDS: 30-0443).[38] After the phosphorization process, the color of Co@NF changed from dark blue to black. The cobalt phosphate species mainly consists of CoP (JCPDS: 65-2593)[39] and a trace of Co_2P species (JCPDS: 54-0413), where the XRD patterns of the Ru species cannot be detected due to the low Ru loading as shown in Fig. 2a. However, the pure Ru-species which were synthesized under similar conditions were detected by the XRD pattern shown in Fig. 2b and the patterns are consistent with that of RuP_3 (JCPDS: 78-1268). In addition, the NF was phosphatized and used as a control sample. Small amounts of Ni_2P species (JCPDS: 03-0953) formed on the NF surface (Fig. S2b†). Moreover, none of the diffraction peaks of NF and Ni_2P appeared on Co modified NF indicating a full surface coverage of NF. Therefore, the contribution of Ni_2P towards the catalytic performance of RuP_3–CoP is negligible. As shown in Fig. 2c, the SEM images are used to distinguish the morphological changes of NF before and after deposition. The surface morphology of NF changes dramatically from the relatively smooth surface to highly ring coiled hierarchical structures at the micro level after different electrodeposition times, indicating the formation of $Co(OH)_2$ nanosheets on the NF surface which becomes denser upon increase of the deposition time (Fig. 2d and S3†). After phosphorization at 350 °C, the vertically oriented hierarchical structure starts to shrink because of the crystal structure transformation from amorphous to crystalline. Similar phenomena are observed on both CoP@NF and Co–Ru–P@NF (Fig. 2e and f). The hierarchical structures not only provide a high surface area thereby promoting a better mass transfer but also expose more active sites. Therefore, a high catalytic performance is expected. Moreover, the N_2 adsorption–desorption isotherms at 77 K of Co–Ru–P@NF catalysts with different loadings of Ru species were used to investigate the Brunauer–Emmett–Teller (BET) surface area. The results revealed that when the loading of Ru in the Co–Ru–P@NF is 0.197 mg cm^{-2}, the BET surface area is 11.4 $m^2\ g^{-1}$, and when the loading of Ru is 0.455 mg cm^{-2}, the BET surface area is 13.3 $m^2\ g^{-1}$ (Fig. S4†).

To further examine the microscopic features of the Co–Ru–P@NF, detailed TEM studies were undertaken. As shown in Fig. 3a, the RuP_3 nanoclusters with an average particle size of 2.6 nm are uniformly dispersed on the surface of CoP nanosheets. The crystal structures of both CoP and RuP_3 are confirmed in Fig. 3b where the distinct lattice fringe with a spacing of 0.28 nm corresponds to the (111) plane of CoP, and the two closely related spacings of 0.25 and 0.39 nm are attributed to the (002) and (110) planes of RuP_3, respectively. Furthermore, the HAADF-STEM (Fig. 3c) and corresponding elemental mapping images reveal the homogenous distribution of Ru, Co, and P in the Co–Ru–P nanostructures. Notably, the much sparser Ru dispersion patterns are consistent with features of the low content Ru-based material in the hybrid composite.

3.3. XPS analysis

The chemical states of each element in Co–Ru–P@NF are further analyzed by XPS, where the Ni cannot be detected on the

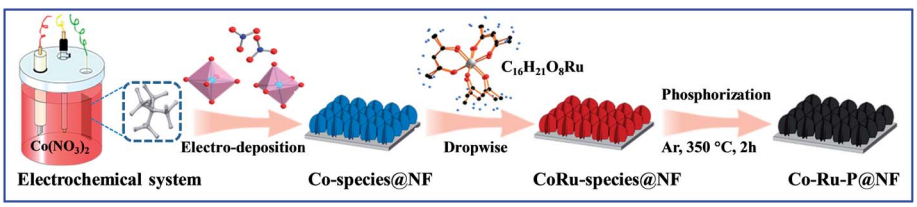

Fig. 1 Schematic diagram of the formation of the Co–Ru–P@NF catalyst.

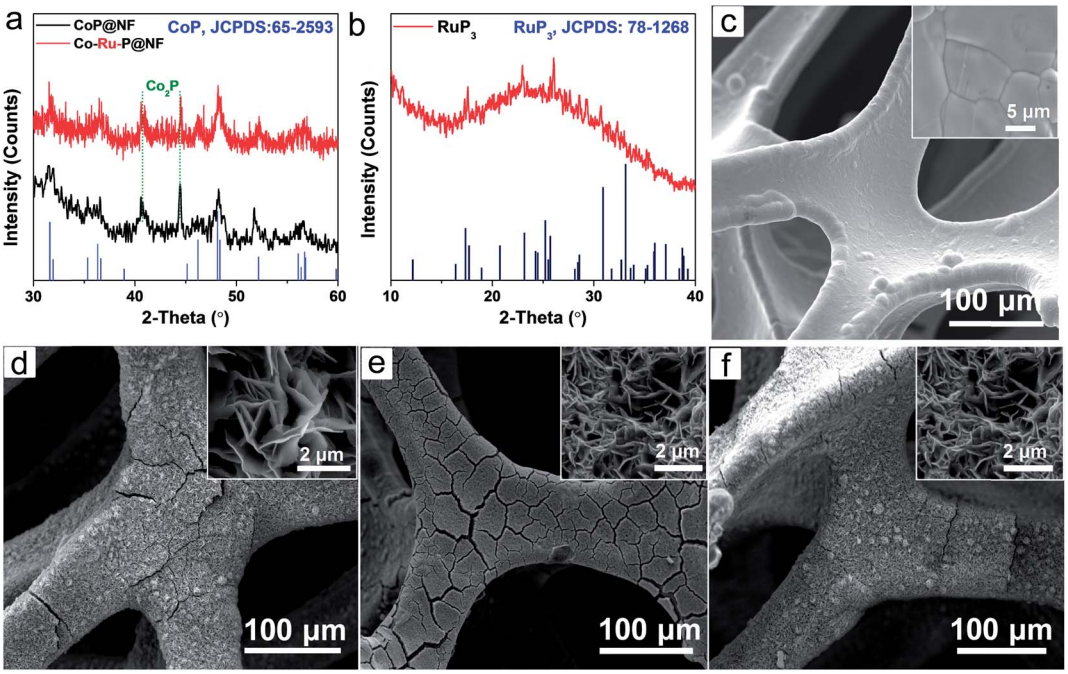

Fig. 2 X-ray diffraction (XRD) patterns of (a) CoP@NF and Co–Ru–P@NF along with (b) RuP_3. Scanning electron microscopy (SEM) images of (c) NF, (d) Co-species@NF, (e) CoP@NF and (f) Co–Ru–P@NF. The insets show the magnified SEM images.

surface of the Co–Ru–P@NF (Fig. S5†), which not only shows a uniform deposition of Co but also indicates that the Co film is thicker than the penetration depth of XPS (around 10 nm). The high-resolution XPS spectra of C 1s + Ru 3d regions (Fig. 4a) are convoluted into C–C (284.8 eV) and C–O (286.0 eV) used as calibration standards,[40,41] and the Ru 3d core levels from RuP_3 are convoluted at the binding energies of 280.8 eV (Ru $3d_{5/2}$) and 285.0 eV (Ru $3d_{3/2}$).[42] As shown in Fig. 4b, three peaks in the Co $2p_{3/2}$ regions at 778.3, 782.0 and 785.5 eV can be ascribed to the Co–P, Co–O and satellite peak, respectively.[43] In addition, the high-resolution XPS spectrum of the P 2p core level shows three types of peaks, where a pair of peaks located at 129.1 eV (P $2p_{3/2}$) and 130.1 eV (P $2p_{1/2}$) are attributed to P 2p in CoP.[44] The another pair of peaks located at 129.7 eV (P $2p_{3/2}$) and 130.8 eV (P $2p_{1/2}$) are attributed to P 2p in RuP_3,[45] along with a broad peak at 133.6 eV assigned to phosphate species.[46] These distinct

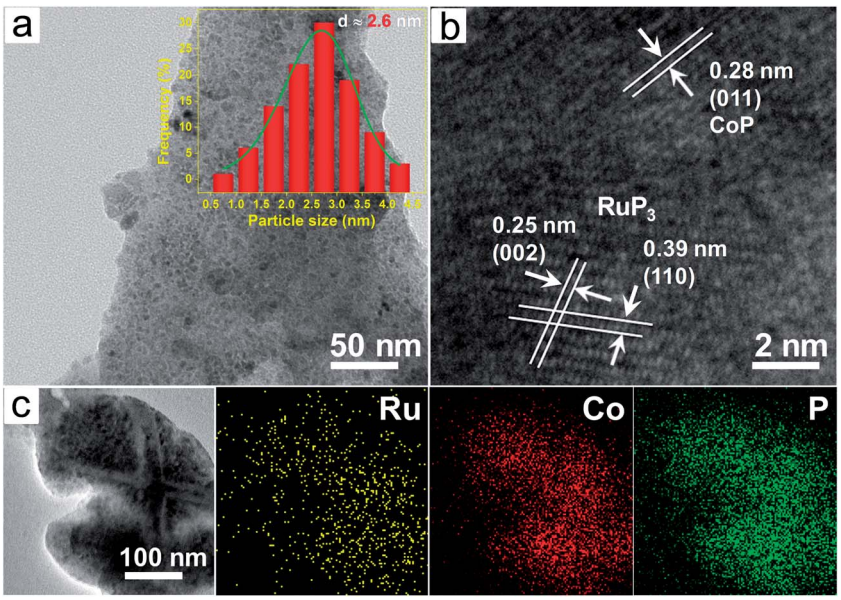

Fig. 3 (a) Transmission electron microscopy (TEM) and (b) high-resolution TEM images of the Co–Ru–P material. The inset of (a) shows the particle size distribution of RuP_3. (c) Typical TEM image of Co–Ru–P and the corresponding Ru, Co and P elemental mappings.

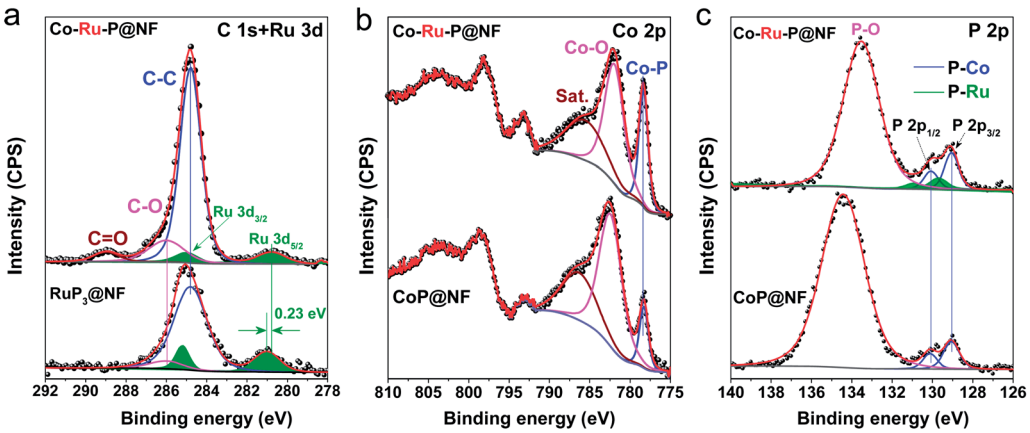

Fig. 4 High-resolution X-ray photoelectron spectroscopy (XPS) of (a) C 1s + Ru 3d, (b) Co 2p and (c) P 2p regions of Co–Ru–P@NF, RuP_3@NF and CoP@NF.

oxidation species peaks of Co–O and P–O can be explained by the inevitable surface oxidation.[47] We have compared the high-resolution Ru 3d XPS spectra of RuP_3@NF and Co–Ru–P@NF in Fig. 4a. The results show that the binding energy of Ru 3d of Co–Ru–P@NF exhibits a negative shift of *ca.* 0.23 eV compared to that of RuP_3@NF indicating higher electron density on Ru in the Co–Ru–P@NF as compared to that of RuP_3@NF due to the partial electron transfer from Co species indicating that the electron density on Ru species is lower than that of Co species. However, almost no shift was observed in the case of Co 2p because Ru amounts are so small and consequently the charge transfer is not significant enough to cause the shift of the Co 2p signal.

3.4. Catalytic hydrolysis analysis

The H_2 production of $NaBH_4$ hydrolysis using the designed catalysts was performed in alkaline $NaBH_4$ solution at 25 °C. The schematic illustration of the experimental setup is shown in Fig. S6,† where the amounts of the generated H_2 were calculated according to the weight of the water displaced by H_2. The effect of electrodeposition of CoP at various times on the H_2 production was investigated as shown in Fig. 5a and b. The results show that the H_2 generation rate is gradually increased with the prolonged deposition times and the 60 min deposition time was selected as the basis of all the other experiments performed below. In addition, the optimal Ru loading was investigated by altering the deposition methods such as drop

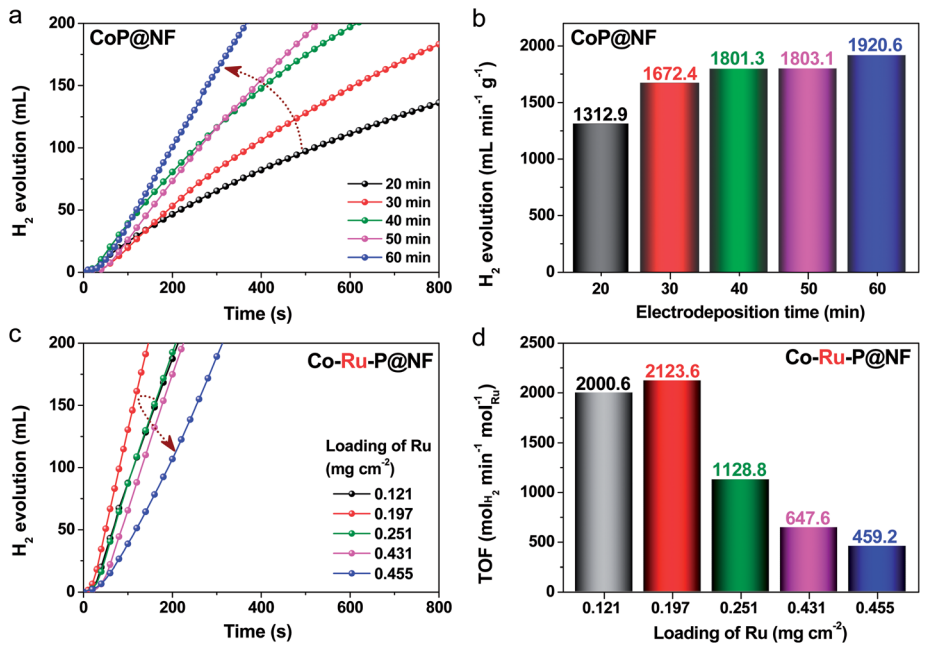

Fig. 5 (a) The relationship between the H_2 generation rates and electro-deposition times of CoP@NF catalysts, and (b) the summarized TOF values. (c) The relationship between the H_2 generation rates and loadings of Ru species on Co–Ru–P@NF catalysts, and (d) the summarized TOF values. All the experiments were conducted in 150 mM $NaBH_4$ + 0.4 wt% NaOH at 25 °C.

casting and dip coating as well as the use of several Ru precursors including $C_{15}H_{21}O_6Ru$, $RuCl_2$ and Ru nanoparticles (Fig. S7†). Then, the catalytic performance of the resulting catalysts on H_2 generation was monitored (Fig. S8†). Finally, the best catalytic performance was achieved by using ethanol solution of $C_{15}H_{21}O_6Ru$ through a drop casting method. The optimal loading is around 0.2 mg (Ru) cm^{-2} measured by ICP-AES (Tables S1 and S2†) and the overall Ru loading against Co is around 1.57 wt% (0.09 mol%). The corresponding TOF for the fastest hydrogen evolution rate (4840 mL min^{-1} $g_{catalyst}{}^{-1}$) is 2123.6 mol min^{-1} $mol_{Ru}{}^{-1}$, which is the highest TOF value reported so far among all the $NaBH_4$ hydrolysis catalysts (Table S3†). This outstanding catalytic performance can be related to the high surface roughness that exposes more active sites, uniform distribution of the active sites and synergic effect between Ru and Co.

To further evaluate this synergetic effect, a comparison study of $NaBH_4$ decomposition was performed between all the intermediate catalysts including CoP@NF, RuP_3@NF, Co-species@NF, Ni_2P@NF and NF. The results show that the hydrogen generation rate of 1.57 wt% Ru loaded CoP@NF is significantly higher than those of CoP@NF and RuP_3@NF (Fig. S9†). Meanwhile, the NF and Ni_2P@NF show almost no activity towards H_2 generation towards $NaBH_4$ hydrolysis (Fig. 6a). The specific H_2 evolution rate of Co–Ru–P@NF is 4839.8 mL min^{-1} $g_{cat}{}^{-1}$ (total mass of the catalyst), which is 2.52 and 23.55 fold higher than those of CoP@NF and RuP_3@NF respectively. To measure the activation energies, a set of experiments were conducted at different temperatures using the two most active catalysts the Co–Ru–P@NF and the CoP@NF. As shown in Fig. S10 and S11,† the rate of H_2 generation increases rapidly with increasing the reaction temperatures from 298 K to 318 K, and the rate constant κ is calculated from the initial slope of each experiment. The activation energy of the Co–Ru–P@NF catalyst is calculated to be 40.3 kJ mol^{-1} using the Arrhenius plot ($\ln \kappa$ *vs.* $1/T$), which is much lower than that of CoP@NF (56.1 kJ mol^{-1}) (Fig. 6b), implying a kinetically enhanced catalytic activity towards $NaBH_4$ hydrolysis to produce H_2 owing to the Ru.[48]

The stability of the optimized Co–Ru–P@NF catalyst was evaluated by the continuous recycling experiments of the $NaBH_4$ hydrolysis in basic solution. The catalyst was cleaned, freeze-dried and weighed after each cycle. The results show almost no changes in catalytic performance after five consecutive cycles after normalizing to the catalyst-mass (Fig. 6c and d). However, the time required to reach 500 mL of H_2 was increased from 5.9 to 13.9 min after five cycles. The catalyst deactivation could be ascribed to the RuP_3 exfoliation, structural damage and catalyst poisoning by $BO_2{}^-$ species (Fig. S12 and S13†).[49]

3.5. Catalytic mechanism analysis

As mentioned above, the high catalytic activities of Co–Ru–P@NF series are directly related to the synergetic effect between Ru and Co along with the unique morphology associated with the large surface area and the open-channels for effective mass transport. The negative shift of the Ru 3d binding energy in XPS caused by the partial electron transfer from Co species to Ru species indicates a higher electron density on Co species as compared to that of Ru species. Accordingly, the partially electronegative hydrogen atoms preferred to attach to the Ru^{3+} atoms. As a result, the $BH_4{}^-$ undergoes a reversible dissociation on Co and Ru metal sites where the hydrogen atom adsorbs on Ru and BH_3 attaches to the Co species. The negatively charged

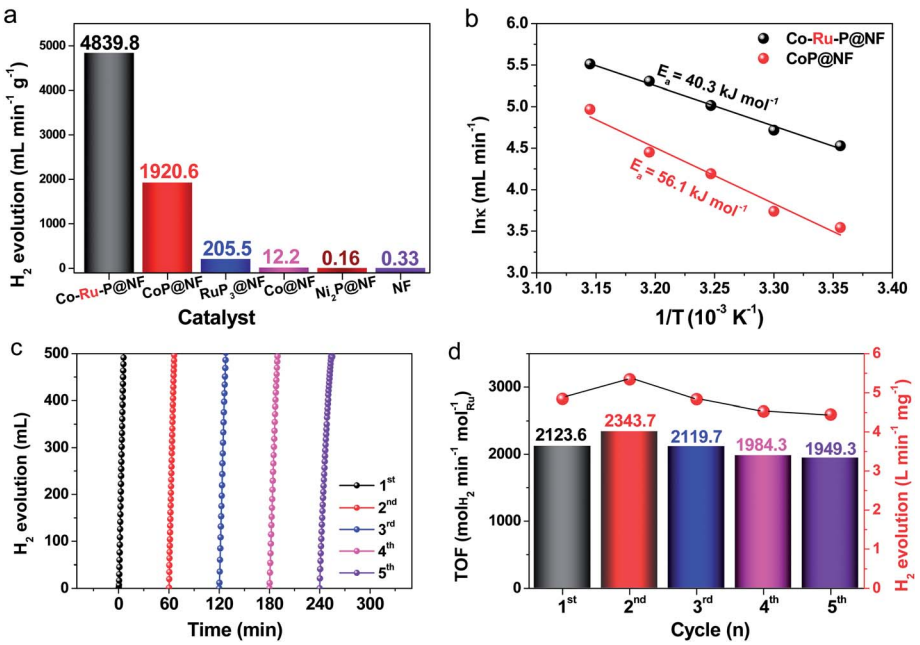

Fig. 6 (a) The summarized TOF values of different catalysts for hydrolysis of 150 mM $NaBH_4$ + 0.4 wt% NaOH solution at 25 °C. (b) The summarized Arrhenius plots of CoP@NF and Co–Ru–P@NF at different reaction temperatures for alkaline $NaBH_4$ hydrolysis. (c) Recycling stability test of the Co–Ru–P@NF catalyst in 150 mM $NaBH_4$ + 0.4 wt% NaOH at 25 °C. (d) The specific H_2 evolution rates and the corresponding TOF values of the Co–Ru–P@NF catalyst in different recycling tests.

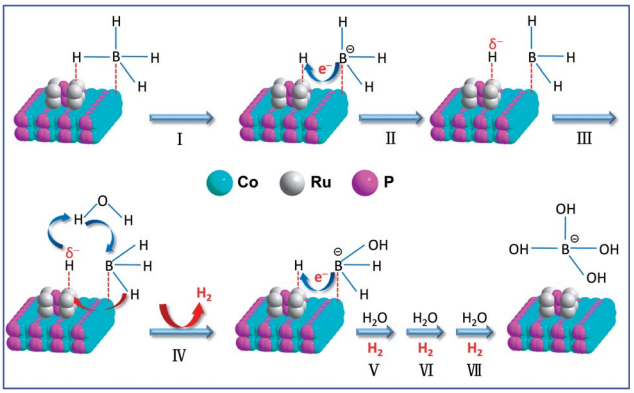

Fig. 7 Catalytic mechanism diagram of the Co–Ru–P@NF catalyst for H_2 generation by hydrolysis of alkaline $NaBH_4$ solution.

boron species transfer the electron to Ru through the conductive bulk and then the partially negatively charged hydrogen atom on the Ru surface extracts a hydrogen from water while the OH ion attacks the BH_3 to release a H_2 molecule followed by transferring one hydrogen atom of the BH_3 to the free Ru site. The surface adsorbed $BH_2(OH)$ species forms after one cycle. The reaction continues until all the hydrogen atoms are replaced by OH ions and then the $B(OH)_4^-$ leaves the surface (Fig. 7).[50]

4. Conclusion

In summary, we have successfully developed a simple and novel strategy to fabricate hierarchical structures of RuP_3 loaded CoP@NF nanosheets for H_2 generation by $NaBH_4$ hydrolysis in alkaline solution. The XRD, XPS and TEM analysis of the Co–Ru–P@NF material show that the RuP_3 nanoclusters are uniformly dispersed on the surface of the vertically grown CoP nanosheets on the NF, which creates channels for rapid mass transfer and sufficient exposure of the active sites. The resultant Co–Ru–P@NF catalyst exhibits an exceptionally high TOF value of 2123.6 mol_{H_2} min^{-1} $mol_{Ru}{}^{-1}$ at 25 °C, which is one of the highest results reported so far. The superior catalytic activity is in strong agreement with the low activation energy (40.3 kJ mol^{-1}). Additionally, the Co–Ru–P@NF catalyst showed a slight decay of around 8.2% after five cycles demonstrating a good stability towards $NaBH_4$ hydrolysis. Furthermore, this study might shed light on designing a metal-phosphide based catalyst for $NaBH_4$ hydrolysis with high activity, good durability, and reusability.

Conflicts of interest

There are no conflicts to declare.

Acknowledgements

This work has been supported by the National Natural Science Foundation of China (21363003, 21165004, and 21163002), Natural Science Foundation of Guangxi Province (2018GXNSFAA294077 and 2017GXNSFGA198004), BAGUI scholar program (2014A001) and Project of Talents Highland of Guangxi Province.

Notes and references

1 X. Zhang, Y. Zhao, X. Jia, Y. Zhao, L. Shang, Q. Wang, G. I. N. Waterhouse, L.-Z. Wu, C.-H. Tung and T. Zhang, *Adv. Energy Mater.*, 2018, **8**, 1702780.
2 J. Chen, Z.-H. Lu, Q. Yao, G. Feng and Y. Luo, *J. Mater. Chem. A*, 2018, **6**, 20746–20752.
3 D. G. Tong, D. M. Tang, W. Chu, G. F. Gu and P. Wu, *J. Mater. Chem. A*, 2013, **1**, 6425–6432.
4 N. Sahiner and S. Demirci, *Appl. Catal., B*, 2017, **202**, 199–206.
5 T. Liu, K. Wang, G. Du, A. M. Asiri and X. Sun, *J. Mater. Chem. A*, 2016, **4**, 13053–13057.
6 H.-L. Wang, J.-M. Yan, Z.-L. Wang, S.-I. O and Q. Jiang, *J. Mater. Chem. A*, 2013, **1**, 14957–14962.
7 Y. Li, T. Gao, Y. Yao, Z. Liu, Y. Kuang, C. Chen, J. Song, S. Xu, E. M. Hitz, B. Liu, R. J. Jacob, M. R. Zachariah, G. Wang and L. Hu, *Adv. Energy Mater.*, 2018, **8**, 1801289.
8 C. Tang, L. Xie, K. Wang, G. Du, A. M. Asiri, Y. Luo and X. Sun, *J. Mater. Chem. A*, 2016, **4**, 12407–12410.
9 Q. Yao, Z.-H. Lu, W. Huang, X. Chen and J. Zhu, *J. Mater. Chem. A*, 2016, **4**, 8579–8583.
10 F. Fu, C. Wang, Q. Wang, A. M. Martinez-Villacorta, A. Escobar, H. Chong, X. Wang, S. Moya, L. Salmon, E. Fouquet, J. Ruiz and D. Astruc, *J. Am. Chem. Soc.*, 2018, **140**, 10034–10042.
11 H. Zhang, G. Xia, J. Zhang, D. Sun, Z. Guo and X. Yu, *Adv. Energy Mater.*, 2018, **8**, 1702975.
12 Z. Zhang, S. Zhang, Q. Yao, X. Chen and Z.-H. Lu, *Inorg. Chem.*, 2017, **56**, 11938–11945.
13 A. Kantürk Figen, K. Taşçi and B. Coşkuner Filiz, *Kinet. Catal.*, 2018, **59**, 128–135.
14 C. Wu, J. Zhang, J. Guo, L. Sun, J. Ming, H. Dong, Y. Zhao, J. Tian and X. Yang, *ACS Sustainable Chem. Eng.*, 2018, **6**, 7451–7457.
15 C. Wu, J. Guo, J. Zhang, Y. Zhao, J. Tian, T. T. Isimjan and X. Yang, *Renewable Energy*, 2019, DOI: 10.1016/j.renene.2018.09.070.
16 A. Lale, A. Wasan, R. Kumar, P. Miele, U. B. Demirci and S. Bernard, *Int. J. Hydrogen Energy*, 2016, **41**, 15477–15488.
17 J.-X. Kang, T.-W. Chen, D.-F. Zhang and L. Guo, *Nano Energy*, 2016, **23**, 145–152.
18 M. Irum, M. Zaheer, M. Friedrich and R. Kempe, *RSC Adv.*, 2016, **6**, 10438–10441.
19 Q. Yao, W. Shi, G. Feng, Z.-H. Lu, X. Zhang, D. Tao, D. Kong and X. Chen, *J. Power Sources*, 2014, **257**, 293–299.
20 H. X. Nunes, M. J. F. Ferreira, C. M. Rangel and A. M. F. R. Pinto, *Int. J. Hydrogen Energy*, 2016, **41**, 15426–15432.
21 L. Wang, L. Huang, C. Jiao, Z. Huang, F. Liang, S. Liu, Y. Wang and H. Zhang, *Catalysts*, 2017, **7**, 25.
22 L. Wei and Z. Yuan, *AIP Conf. Proc.*, 2017, **1794**, 020004.

23 C. Li, D. Wang, Y. Wang, G. Li, G. Hu, S. Wu, Z. Cao and K. Zhang, *J. Colloid Interface Sci.*, 2018, **524**, 25–31.
24 F. Wang, Y. Zhang, Y. Wang, Y. Luo, Y. Chen and H. Zhu, *Int. J. Hydrogen Energy*, 2018, **43**, 8805–8814.
25 Y. Zou, Y. Yin, Y. Gao, C. Xiang, H. Chu, S. Qiu, E. Yan, F. Xu and L. Sun, *Int. J. Hydrogen Energy*, 2018, **43**, 4912–4921.
26 Q. Li, W. Yang, F. Li, A. Cui and J. Hong, *Int. J. Hydrogen Energy*, 2018, **43**, 271–282.
27 K. A. Holbrook and P. J. Twist, *J. Chem. Soc. A*, 1971, 890–894.
28 C.-C. Hou, Q. Li, C. Wang, C.-Y. Peng, Q.-Q. Chen, H.-F. Ye, W. Fu, C.-M. Che and N. Lopez, *Energy Environ. Sci.*, 2017, **10**, 1770–1776.
29 C. Tang, R. Zhang, W. Lu, L. He, X. Jiang, A. M. Asiri and X. Sun, *Adv. Mater.*, 2017, **29**, 1602441.
30 Y. Wei, Y. Wang, L. Wei, X. Zhao, X. Zhou and H. Liu, *Int. J. Hydrogen Energy*, 2018, **43**, 592–600.
31 L. He, D. Zhou, Y. Lin, R. Ge, X. Hou, X. Sun and C. Zheng, *ACS Catal.*, 2018, **8**, 3859–3864.
32 A. H. Tamboli, S. W. Gosavi, C. Terashima, A. Fujishima, A. A. Pawar and H. Kim, *Chemosphere*, 2018, **202**, 669–676.
33 X. Peng, D. Chen, X. Yang, D. Wang, M. Li, C.-C. Tseng, R. Panneerselvam, X. Wang, W. Hu, J. Tian and Y. Zhao, *ACS Appl. Mater. Interfaces*, 2016, **8**, 33673–33680.
34 L. Cui, Y. Xu, L. Niu, W. Yang and J. Liu, *Nano Res.*, 2017, **10**, 595–604.
35 L. Wei, M. Ma, Y. Lu, S. Zhang, J. Gao and X. Dong, *Funct. Mater. Lett.*, 2017, **10**, 1750065.
36 K. Mori, K. Miyawaki and H. Yamashita, *ACS Catal.*, 2016, **6**, 3128–3135.
37 Q. Yao, Z.-H. Lu, Y. Yang, Y. Chen, X. Chen and H.-L. Jiang, *Nano Res.*, 2018, **11**, 4412–4422.
38 X. Yang, H. Li, A.-Y. Lu, S. Min, Z. Idriss, M. N. Hedhili, K.-W. Huang, H. Idriss and L.-J. Li, *Nano Energy*, 2016, **25**, 42–50.
39 X. Yang, A.-Y. Lu, Y. Zhu, M. N. Hedhili, S. Min, K.-W. Huang, Y. Han and L.-J. Li, *Nano Energy*, 2015, **15**, 634–641.
40 T. Tang, Q. Gan, X. Guo, H. Dong, J. Zhang, Y. Zhao, J. Tian and X. Yang, *Sustainable Energy Fuels*, 2018, **2**, 229–236.
41 Y. Zeng, S. Tian, D. Wang, H. Dong, X. Cheng, Y. Zhao, J. Tian and X. Yang, *ChemistrySelect*, 2017, **2**, 9291–9297.
42 C. Jing-Qi, G. Wen-Kun, L. Jia-Hui, D. Bin, Y. Kai-Li, Q. Jun-Feng, L. Bin, C. Yong-Ming and L. Chen-Guang, *ChemSusChem*, 2018, **11**, 743–752.
43 S. Liu, Q. Liu, Y. Lv, B. Chen, Q. Zhou, L. Wang, Q. Zheng, C. Che and C. Chen, *Chem. Commun.*, 2017, **53**, 13153–13156.
44 W. Gao, M. Yan, H.-Y. Cheung, Z. Xia, X. Zhou, Y. Qin, C.-Y. Wong, Y. Qu, C.-R. Chang and J. C. Ho, *Nano Energy*, 2017, **38**, 290–296.
45 Z. Pu, I. S. Amiinu, Z. Kou, W. Li and S. Mu, *Angew. Chem., Int. Ed.*, 2017, **56**, 11559–11564.
46 H. Zhang, X. Li, A. Hähnel, V. Naumann, C. Lin, S. Azimi, S. L. Schweizer, A. W. Maijenburg and R. B. Wehrspohn, *Adv. Funct. Mater.*, 2018, **28**, 1706847.
47 S. Cao, Y. Chen, H. Wang, J. Chen, X. Shi, H. Li, P. Cheng, X. Liu, M. Liu and L. Piao, *Joule*, 2018, **2**, 549–557.
48 D. Kılınç, Ö. Şahin and C. Saka, *Int. J. Hydrogen Energy*, 2018, **43**, 251–261.
49 L. Zhou, J. Meng, P. Li, Z. Tao, L. Mai and J. Chen, *Mater. Horiz.*, 2017, **4**, 268–273.
50 U. B. Demirci and P. Miele, *C. R. Chim.*, 2014, **17**, 707–716.